Inversion-recovery MR elastography of the human brain for improved stiffness quantification near fluid–solid boundaries

Ledia Lilaj[1] | Helge Herthum[1] | Tom Meyer[1] | Mehrgan Shahryari[1] |
Gergely Bertalan[1] | Alfonso Caiazzo[2] | Jürgen Braun[3] | Thomas Fischer[1] |
Sebastian Hirsch[4,5] | Ingolf Sack[1]

[1]Department of Radiology, Charité–Universitätsmedizin Berlin, Berlin, Germany

[2]Weierstrass Institute for Applied Analysis and Stochastics, Berlin, Germany

[3]Institute of Medical Informatics, Charité–Universitätsmedizin Berlin, Berlin, Germany

[4]Berlin Center for Advanced Neuroimaging, Charité–Universitätsmedizin Berlin, Berlin, Germany

[5]Bernstein Center for Computational Neuroscience, Berlin, Germany

Correspondence
Ingolf Sack, Department of Radiology,
Charité–Universitätsmedizin Berlin,
Charitéplatz 1, 10117 Berlin, Germany.
Email: Ingolf.sack@charite.de

Purpose: In vivo MR elastography (MRE) holds promise as a neuroimaging marker. In cerebral MRE, shear waves are introduced into the brain, which also stimulate vibrations in adjacent CSF, resulting in blurring and biased stiffness values near brain surfaces. We here propose inversion-recovery MRE (IR-MRE) to suppress CSF signal and improve stiffness quantification in brain surface areas.

Methods: Inversion-recovery MRE was demonstrated in agar-based phantoms with solid-fluid interfaces and 11 healthy volunteers using 31.25-Hz harmonic vibrations. It was performed by standard single-shot, spin-echo EPI MRE following 2800-ms IR preparation. Wave fields were acquired in 10 axial slices and analyzed for shear wave speed (SWS) as a surrogate marker of tissue stiffness by wavenumber-based multicomponent inversion.

Results: Phantom SWS values near fluid interfaces were $7.5 \pm 3.0\%$ higher in IR-MRE than MRE ($P = .01$). In the brain, IR-MRE SNR was 17% lower than in MRE, without influencing parenchymal SWS (MRE: 1.38 ± 0.02 m/s; IR-MRE: 1.39 ± 0.03 m/s; $P = .18$). The IR-MRE tissue–CSF interfaces appeared sharper, showing 10% higher SWS near brain surfaces (MRE: 1.01 ± 0.03 m/s; IR-MRE: 1.11 ± 0.01 m/s; $P < .001$) and 39% smaller ventricle sizes than MRE ($P < .001$).

Conclusions: Our results show that brain MRE is affected by fluid oscillations that can be suppressed by IR-MRE, which improves the depiction of anatomy in stiffness maps and the quantification of stiffness values in brain surface areas. Moreover, we measured similar stiffness values in brain parenchyma with and without fluid suppression, which indicates that shear wavelengths in solid and fluid compartments are identical, consistent with the theory of biphasic poroelastic media.

1 | INTRODUCTION

Cerebral stiffness quantified by in vivo MR elastography (MRE) is an emerging imaging marker of structural changes in neural tissue.[1-3] This technique uses extrinsically actuated shear waves as a contrast medium to measure the viscoelastic response of soft tissues.[4] Shear wave displacement fields are acquired by motion-sensitive phase-contrast imaging sequences and analyzed for shear modulus using inversion routines.[5-7]

Compared with other body tissues, the brain poses special challenges for MRE. For example, the brain is highly heterogeneous with abundant solid-fluid tissue interfaces, has anisotropic and poroelastic properties, and is a pulsatile organ.[8] Consequently, in vivo MRE of the brain is still inferior to MRE of other organs in terms of consistency and reproducibility, and only a few studies have so far reported on the properties of thin tissue layers such as the cerebral cortex.[9]

The brain could be considered a biphasic poroelastic medium composed of a solid phase that includes cells, extracellular compartments, and entrapped interstitial fluid, and a second liquid phase that includes all fluid parts, which can move independently of the solid phase on the time scale of MRE oscillations.[10-13] Conventional MRE encodes solid and fluid phases as a single, averaged, effective displacement field, and therefore cannot differentiate between the contributions of the two phases to tissue stiffness.[14]

In previous work, we have introduced inversion recovery (IR) MRE to selectively suppress signal of the fluid phase in brain tissue, to therefore encode fluid and solid displacement fields separately.[15] Using this technique, we have shown that the human brain, especially gray matter, is a highly poroelastic medium with a porosity of $14 \pm 2\%$ and negative coupling density between solid and fluid phases.[15] However, IR-MRE has never been used to recover stiffness of brain tissue based on the isolated solid displacement field.

Our hypothesis is that IR-MRE can improve quantification of stiffness in brain surface areas by suppressing unwanted signal of fluid motion at interfaces.[16] It is known that fluids near solid boundaries can move in synchrony with solid tissue motion due to the liquid's adhesion to the interface, giving rise to phase-locked fluid–solid displacement fields with wavelengths dictated by the solid's properties.[17] It should be emphasized that, even though the liquid phase does not transmit shear waves, it acts as a "parasitic mass" to the solid matrix, adding a coupling density to the solid's motion.[14] Vice versa, surface waves in the liquid phase cause particle motion to the depth of several wavelengths, and therefore lead to a reflection of the solid-phase properties within the liquid volume. This apparent transition of solid properties into nearby fluid such as CSF at boundaries causes uncertainty in the localization of these boundaries. While fluid vibrations due to nearby boundaries or vessel walls can reveal intrinsic properties of the heart[18-20] or aorta,[21,22] it may be beneficial to suppress signal of these fluid vibrations with IR-MRE in the brain to better delineate tissue values near fluid–solid boundaries.

Our study has three aims: first, to introduce stiffness quantification by IR-MRE of the brain based on solid displacement fields; second, to compare IR-MRE with conventional MRE focusing on brain surface areas; and, third, to assess the sharpness of brain-CSF interfaces based on the extent of sulci and ventricles in IR-MRE stiffness maps. Our overall aim is to estimate the contribution of fluid motion to stiffness in brain MRE maps. It should be emphasized that we do not focus on the distinction between gray and white matter, but on the correct determination of MRE values near brain surfaces, regardless of the underlying anatomy.

Stiffness maps will be generated using wavenumber-based analysis to obtain shear wave speed (SWS). The SWS reconstruction is known to be fairly insensitive to noise,[23,24] which we consider important, as IR-MRE, due to the suppression of fluid signal, has a lower SNR than MRE. Investigators use SWS as a surrogate parameter of stiffness, albeit not synonymous with shear modulus.[6] In this article we will discuss stiffness based on SWS in a narrative context but use SWS in meters per second for tabulating quantitative values.

2 | METHODS

To demonstrate the effect of fluid motion on adjacent solid tissue in MRE stiffness maps, we produced four biphasic fluid–solid phantoms by mixing melted agar-based ViroGel (Bego, Bremen, Germany) with water. Three phantoms with a size of 0.8 L were prepared, two of which with 33% wt/vol and one with 50% wt/vol, while one phantom was made with a size of 1.5 L and a concentration of 50% wt/vol. The solutions were poured into vessels, solidified for 24 hours, and then overlaid with water (Figure 1A). The solid–fluid interface was either left flat or carved with two triangle-shaped incisions to mimic sulci and ventricles. In vivo examinations of the brain were performed in 11 male volunteers without any history of neurological events (mean age $\pm$ SD: 34 ± 12 years, age range: 22-60 years). The institutional review board approved the study. All participants gave written informed consent.
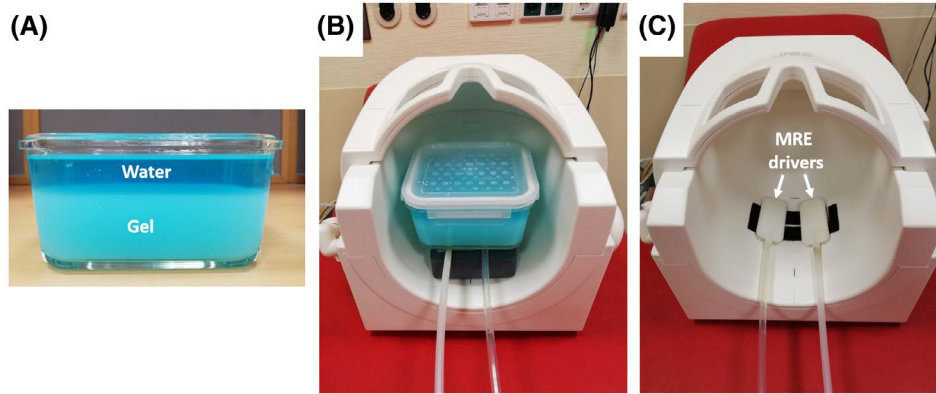
(A) **(B)** **(C)**

FIGURE 1 Experimental setup. A, Phantom consisting of solid and fluid layers to demonstrate fluid–solid motions induced and encoded by MR elastography (MRE) and inversion-recovery (IR) MRE. B, Placement of the phantom in the head RF coil of the MRI scanner on top of two pressurized air actuators. C, Pressurized air actuators for in vivo brain experiments. The head is placed directly on top of the two drivers, to induce lateral (rotational) motion of the head

2.1 | Driver setup

Two compressed air drivers were used to excite oscillatory motion as described in Schrank et al.[25] The drivers were operated with opposite phases in order to maximize lateral motion and minimize motion along the vertical (anterior–posterior) axis. In the phantom experiment, the drivers were placed between a flat plate, which was anchored to the head coil, and the phantom container to ensure optimal transmission of vibrations into the phantom (Figure 1B). Actuator vibration was set to 120.05 Hz at 1 bar. In the in vivo experiment, the back of the volunteer's head was placed directly on the drivers. Vibration frequency was set to 31.25 Hz at 650 mbar (Figure 1C). The frequency range of 30 Hz has been exploited in other studies of brain MRE as a viable compromise between limited wave penetration at higher frequencies and limited wave number at lower frequencies.[26]

2.2 | Magnetic resonance elastography and IR-MRE sequences

The MRE data were acquired with a single-shot, spin-echo EPI sequence as described previously.[15] For IR-MRE, the 90° pulse was preceded by a slice-selective inversion pulse with an inversion time (TI) of 1970 ms in the phantom study and 2800 ms in the in vivo experiments. Both the phantom and volunteers were examined in a 3T MRI scanner (Prisma Fit; Siemens, Erlangen, Germany) using a 32-channel head coil. Ten slices of 110 × 108 matrix size with 2 × 2 × 3 mm resolution were acquired using parallel imaging with GRAPPA factor 2. Echo time and TR were 64 ms and 28,920 ms, respectively. A bipolar, single-cycle motion-encoding gradient (0th moment nulling), single cycle of 8.5 ms and 25 ms duration, and 33 mT/m and 25 mT/m amplitude was used in the phantom and in vivo study, respectively. Total

acquisition time was 24 minutes. A diagram of the IR-MRE sequence is shown in Figure 2.

2.3 | Data processing

In the in vivo experiments of MRE and IR-MRE, displacement and motion artifacts were corrected by performing rigid-body motion correction using the open-source Elastix toolbox as recently described in Shahryari et al.[27] All of the following postprocessing steps were applied equally to the in vivo and phantom data. Phase images were unwrapped using the Laplacian method described in chapter 9.3 of Hirsch et al.[4] Temporal Fourier transform was applied to the components of the time-resolved wave fields to select the fundamental harmonic at vibration frequency, providing three complex-valued components of the wave field. These three shear-wave field components were used to reconstruct shear wave speed (SWS in meters per second), which is proportional to the square root of stiffness contrast. To avoid potential bias due to noise, we used wavenumber-based (k) multicomponent elasto-visco inversion (k-MDEV),[23] which is based on first-order derivatives and therefore has higher fidelity for noisy data than direct-inversion methods based on Laplacian operators.[28] Because k-MDEV inversion was originally introduced for MRE of abdominal organs,[23] we adapted the algorithm by omitting the step of presmoothing of complex MRI data before the temporal Fourier transform, to better preserve abundant fluid–solid interfaces in the brain. Furthermore, the linear radial filter in the spatial frequency domain was replaced by a radial Butterworth bandpass filter of third order with a high-pass threshold of 15/m and low-pass threshold of 200/m. All further postprocessing steps were identical to the k-MDEV method described in Tzschatzsch et al[23] and available online at https://bioqic-apps.charite.de/.

2.4 | Statistical analysis

Regions of interest (ROIs) of surface tissue were automatically selected by thresholding time-averaged MRE magnitude signals, providing binary masks M of brain parenchyma, including CSF in sulci and ventricles. These masks were further treated by erosion of edges in a three-pixel neighborhood. Brain-surface ROIs were finally obtained by subtracting the eroded M from the original M. Mean parenchymal values were quantified over all voxels within M with SWS > 0.9 m/s. Similar empirical SWS thresholds were used in previous MRE studies, because larger fluid-filled regions and blood vessels that appear enlarged in SWS maps are efficiently eliminated.[23,25,26]

The SNR was estimated as the ratio of the magnitude MRE signal between parenchyma and air. Additionally, we quantified the displacement SNR in wave images using the blind noise estimation method proposed by Donoho et al,[29] as outlined and applied to MRE data in Refs 25 and 30. Ventricle sizes were quantified by manual segmentation of the lateral ventricles in three central slices of the SWS maps obtained by MRE and IR-MRE. Statistical significance of the differences between MRE and IR-MRE parameters was tested using the paired Student's t-test with a level of significance of $P = .05$. Statistical tests were performed in *MATLAB* (version 2018; MathWorks, Natick, MA).

3 | RESULTS

3.1 | Phantom study

Figure 3 compares the MRE and IR-MRE in two phantoms. The magnitude signal demonstrates that IR-MRE efficiently suppresses free water signal, leading to a blanked water compartment. Therefore, IR-MRE shows mostly noise in the free water pool, whereas MRE shows waves resulting from the coupling of solid motion to adjacent fluid.[15] Shear waves in the solid compartment were found to have similar amplitudes in MRE and IR-MRE. The SWS maps revealed that mean stiffness values of the solid gel were not different in MRE and IR-MRE (Figure 3A: 4.5 ± 0.3 m/s [MRE], 4.7 ± 0.3
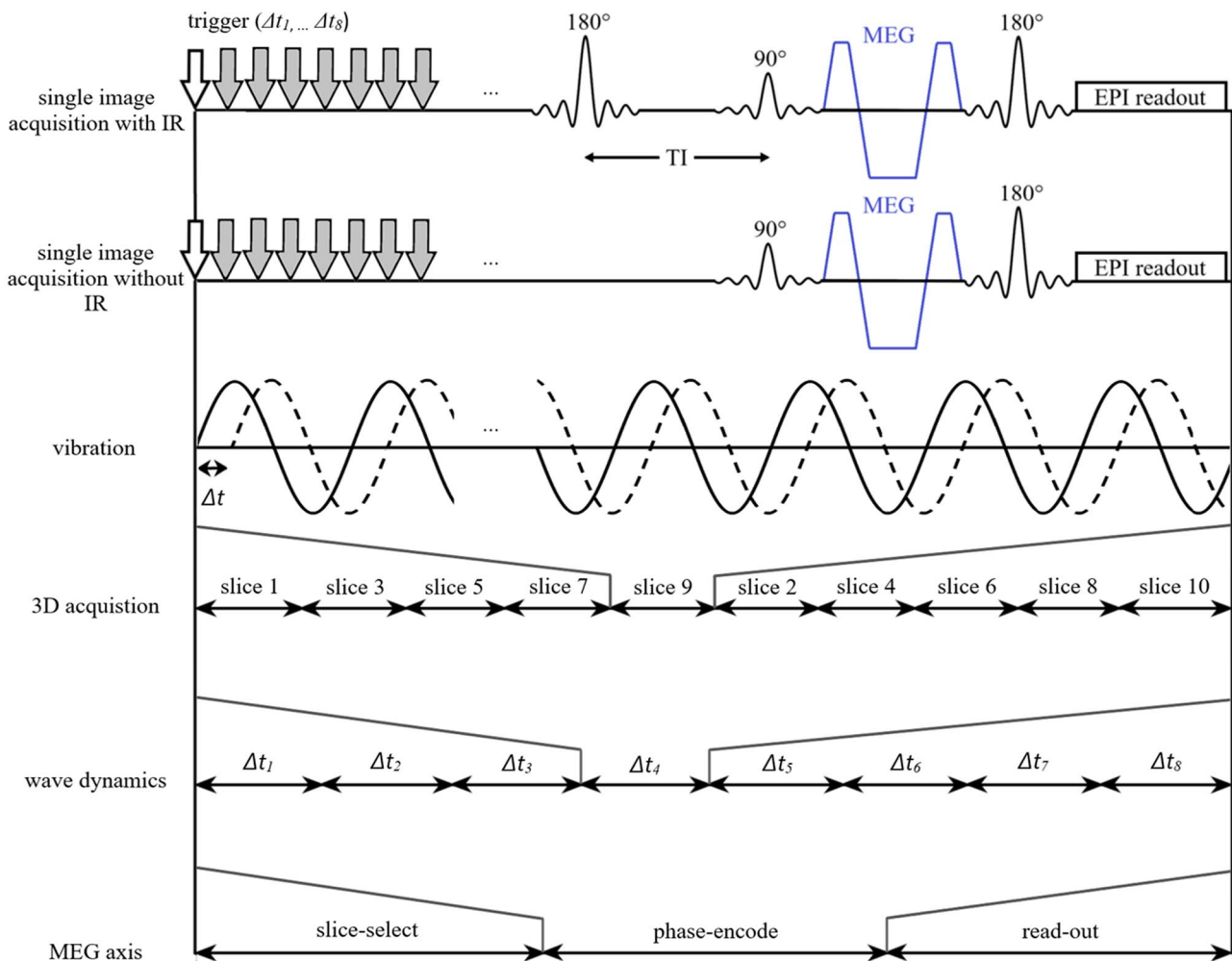

FIGURE 2 Sequence timing diagrams for MRE and IR-MRE used in this study. Note that the time axis is not to scale
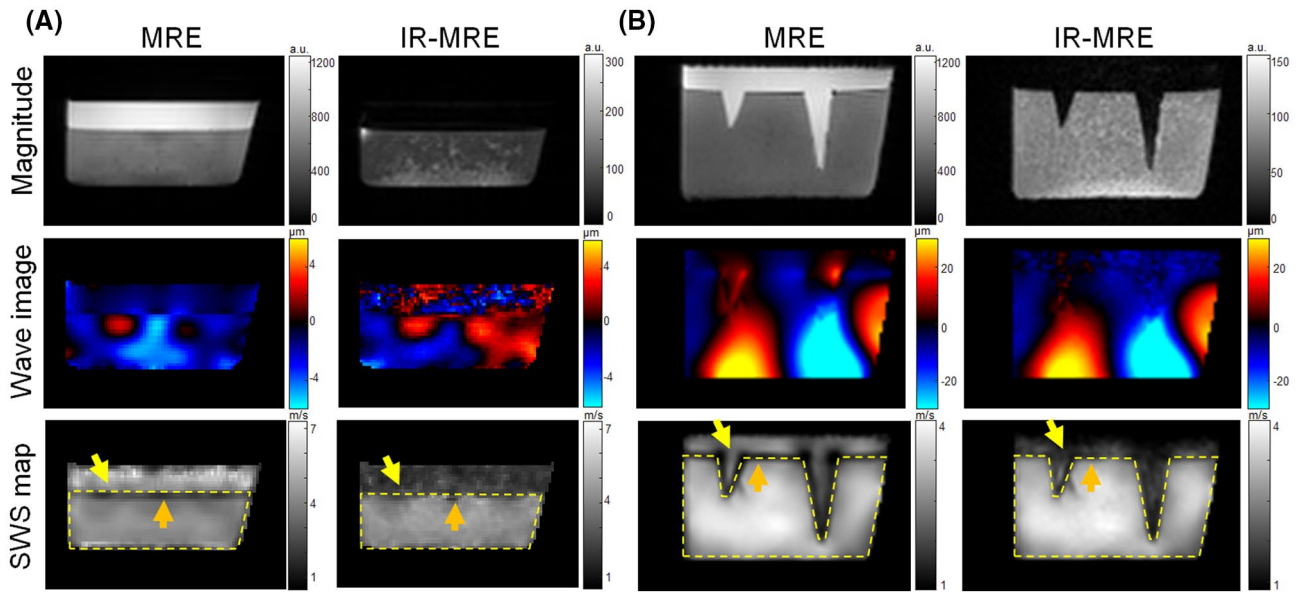
FIGURE 3 Phantoms experiments. The MRE and IR-MRE experiments demonstrate the influence of freely moving water on the appearance of MRE stiffness maps (shear wave stiffness [SWS]) with (IR-MRE) and without suppression (MRE) of fluid signal. Phantoms with plane solid-fluid interface (A) and with two additional cuts mimicking large ventricles and sulci (B). Suppressed liquid signal in IR-MRE appears dark in the SWS maps as opposed to high values in MRE due to surface waves inside the liquid (yellow arrows). Orange arrows demarcate the fluid–solid interface, which appears stiffer in the solid compartment when fluid motion signal is suppressed. Please note the difference in grayscale bars for the magnitude images between MRE and IR-MRE

m/s [IR-MRE], $P = .09$; Figure 3B: 1.8 ± 0.3 m/s [MRE], 1.8 ± 0.3 m/s [IR-MRE], $P = .21$). However, MRE in the free-water compartment showed spuriously high SWS values, whereas IR-MRE, due to the suppression of fluid signal, reflects the ground truth of shear stiffness close to zero in free water (yellow arrows). Furthermore, low SWS intensity was seen at the interface between solid and liquid due to large phase gradients (shear strain) in that area. Obviously, IR-MRE alleviated large phase gradients and improved the spatial representation of SWS values at that interface (orange arrows). Considering all four phantoms, the mean differences between the values of the full phantom in MRE and IR-MRE were small and insignificant ($0.8\% \pm 1.0\%$; $P = .08$), whereas IR-MRE provided on average $7.5\% \pm 3.0\%$ ($P < .001$) higher values in a region of three pixels width close to the interface. Residual variations in SWS intensity at the solid interface may be attributed to the effect of fluid motion as parasitic mass on solid motion, which is not accounted for by standard (monophasic) wave inversion.

3.2 | Volunteer study

Due to the suppression of fluid signal, SNR of the magnitude images was approximately 17% lower in IR-MRE than in MRE (MRE: 355 ± 74; IR-MRE: 296 ± 95; $P < .001$). Surprisingly, displacement SNR of wave images was 7% higher in IR-MRE than MRE (MRE: 28 ± 2 dB; IR-MRE: 30

± 2 dB; $P < .0001$). An example set of wave data is shown in Figure 4. Two main findings are apparent here: First, the orders of shear wave amplitudes were similar in both experiments, although IR-MRE showed slightly lower amplitudes (2.9 ± 0.3 μm) than MRE (3.1 ± 0.3 μm, $P < .001$). Second, as indicated by arrows, phase discontinuities occurred at sulci in MRE and to a lesser extent in IR-MRE, similar to our observations in the phantom. Probably for that reason, displacement SNR was higher in IR-MRE than MRE, as Donoho's method[29] interprets phase discontinuities as "unwanted signal."

A representative set of a surface ROI in MRE and IR-MRE of a volunteer is shown in Figure 5. The SWS values of the entire parenchyma were not significantly different between MRE and IR-MRE (MRE: 1.38 ± 0.02 m/s; IR-MRE: 1.39 ± 0.03 m/s; $P = .18$). Figure 6 shows two slices obtained in a volunteer with MRE and IR-MRE. Tissue–CSF interfaces and sulci appear sharper in IR-MRE than MRE, which is mirrored by 9% higher SWS values in brain surface areas (MRE: 1.01 ± 0.03 m/s; IR-MRE: 1.11 ± 0.01 m/s; $P < .001$) and 39% smaller ventricle sizes than in standard MRE maps ($P < .0001$). Overall parenchyma visible in MRE maps was larger than in IR-MRE maps (MRE: $34\,227 \pm 2763$ voxels; IR-MRE: $33\,004 \pm 3231$ voxels; $P < .001$), whereas the sizes of brain surface masks were smaller in MRE than IR-MRE (MRE: 5361 ± 141 voxels; IR-MRE: 6865 ± 947 voxels; $P < .001$). The increase in brain-surface ROI size due to fluid signal suppression is illustrated in Figure 5, showing
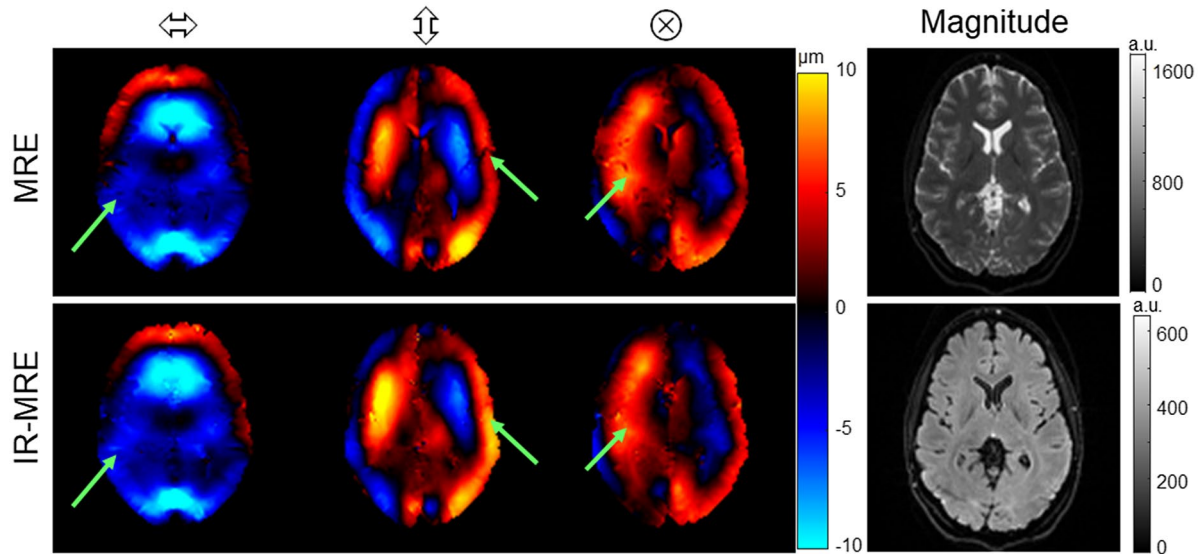
FIGURE 4 Representative wave fields in the brain acquired with MRE and IR-MRE at 31.25 Hz drive frequency and magnitude images for anatomical guidance. Symbols in the column heads indicate the directions of motion encoding. Arrows demarcate phase discontinuities, which appear to be more abundant in MRE than IR-MRE. Please note the difference in grayscale bars for the magnitude images between MRE and IR-MRE
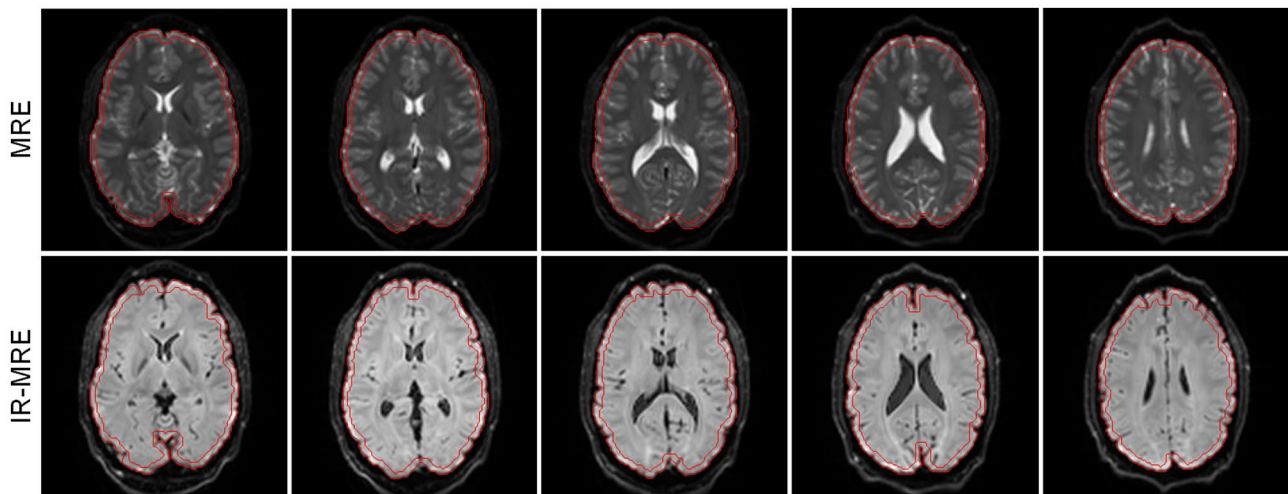

FIGURE 5 Regions of interest (red lines) of the outer-brain surface areas as automatically generated from magnitude signals in MRE and IR-MRE

that these ROIs in volunteers depict more detail of sulci and a higher degree of folded brain surface in maps obtained by IR-MRE compared with conventional MRE. The increase of surface area due to IR-MRE was correlated with an increase in SWS in that region (R = −0.73; P = .01). Applying the same detailed ROI obtained with IR-MRE to conventional MRE still yields higher surface values in IR-MRE than MRE (P = .017).

While the size of the ventricles in IR-MRE was not different from the anatomical ground truth as depicted by T_2-weighted magnitude images (P = .93), it was markedly larger in standard MRE maps (P < .001). The spurious enlargement

of ventricles by MRE is compared with IR-MRE in Figure 7. Group statistical values are plotted in Figure 8.

4 | DISCUSSION

This is the first application of IR-MRE for measuring stiffness in the human brain. The IR-MRE method preserves more detail in brain surface areas and ventricle anatomy than conventional MRE.

Suppression of CSF signal in brain MRE eliminates vibration signals arising from fluid compartments near the
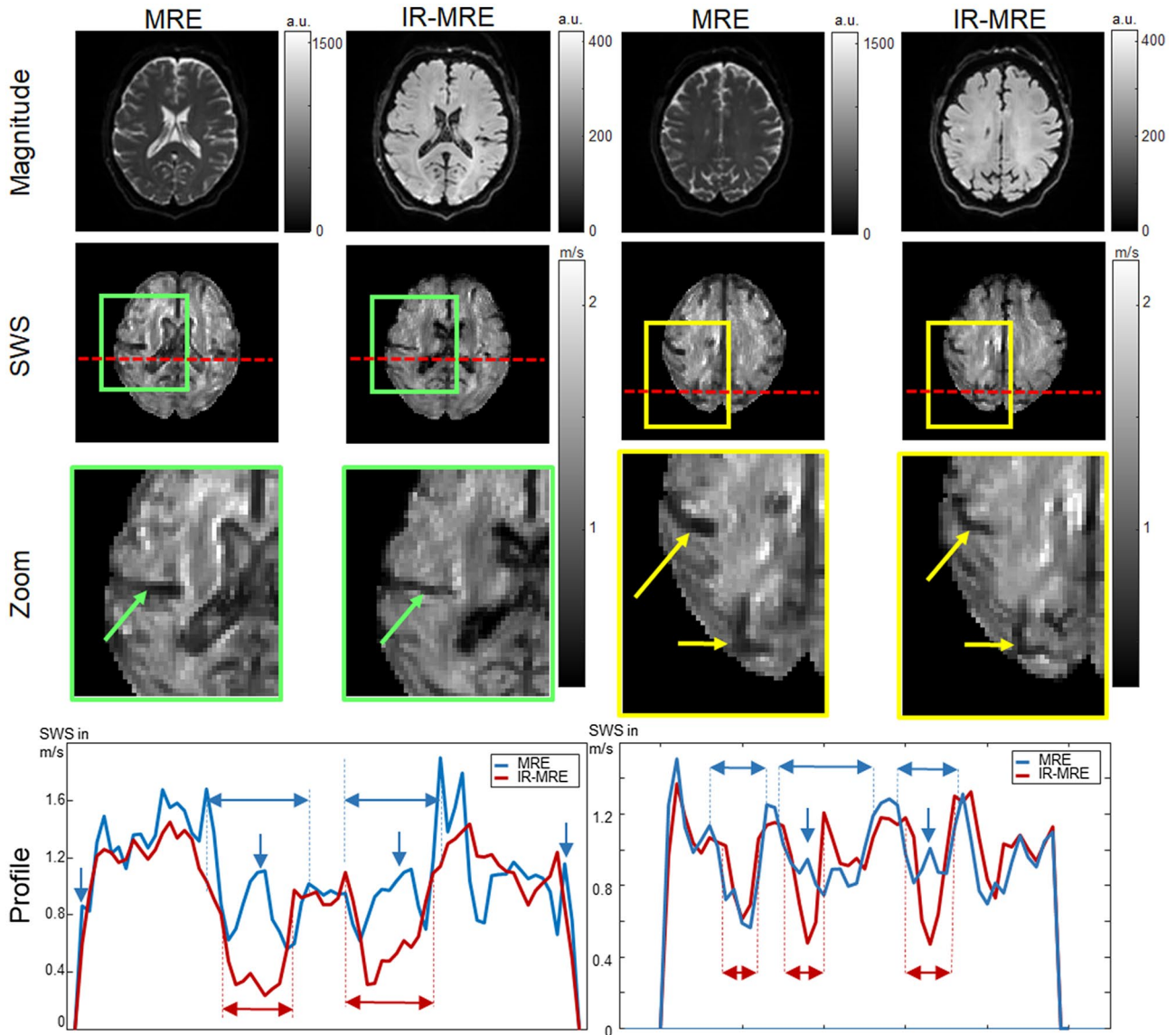
FIGURE 6 Representative brain images obtained by MRE and IR-MRE in the same volunteer. The magnitude signals in IR-MRE, compared with MRE, show solid tissue without freely moving water (note that the relative gray scales are different). This leads to a significantly improved depiction of fluid–solid boundaries in SWS maps, as shown by the green and yellow arrows in the zoomed SWS maps. Note that sulci and ventricles are narrower in IR-MRE than MRE due to suppressed phase discontinuities, similar to the phantom experiments shown in Figure 3. The profiles indicated by the dotted red lines in the SWS maps are shown in the bottom row. The horizontal arrows illustrate the different sizes of ventricles and sulci in MRE and IR-MRE. The vertical arrows indicate spuriously high SWS values in CSF-filled regions

brain surface. As demonstrated by our phantom experiment, fluid signal in MRE mirrors properties of adjacent solid tissue, and therefore displays effective medium properties of solid-like tissue. This effect cannot be suppressed by simply masking out fluid signals before wave inversion. Supporting Information Figure S1 presents such an analysis in the two phantoms shown in Figure 3. It is clearly visible that masking fluid areas and air before inversion leads to artifacts around the phantoms related to discontinuities introduced by the masks. This demonstrates that simple masking of fluid regions does not offer additional insights, whereas IR-MRE improves the characterization of boundaries by intrinsically suppressing the signal of fluid oscillations.

We noted two main effects near fluid–solid interfaces in our conventional MRE brain maps. The first effect is blurring and causes uncertainties in the position of the solid boundary when the adjacent fluid moves in a solid-like fashion. The second is softening due to slip interfaces. High shear strain at nonwelded interfaces is a well-known and long-recognized phenomenon in MRE[16,31] and can be exploited in shear strain–based MRE to differentiate encapsulated brain tumors from tumors with infiltrative growth.[32] As demonstrated in prior work, high shear strain at slip boundaries leads to reconstruction of very low elasticity in the vicinity of the interface.[16] However, most inversion approaches analyze shear strain in a spatially extended neighborhood, causing blurring
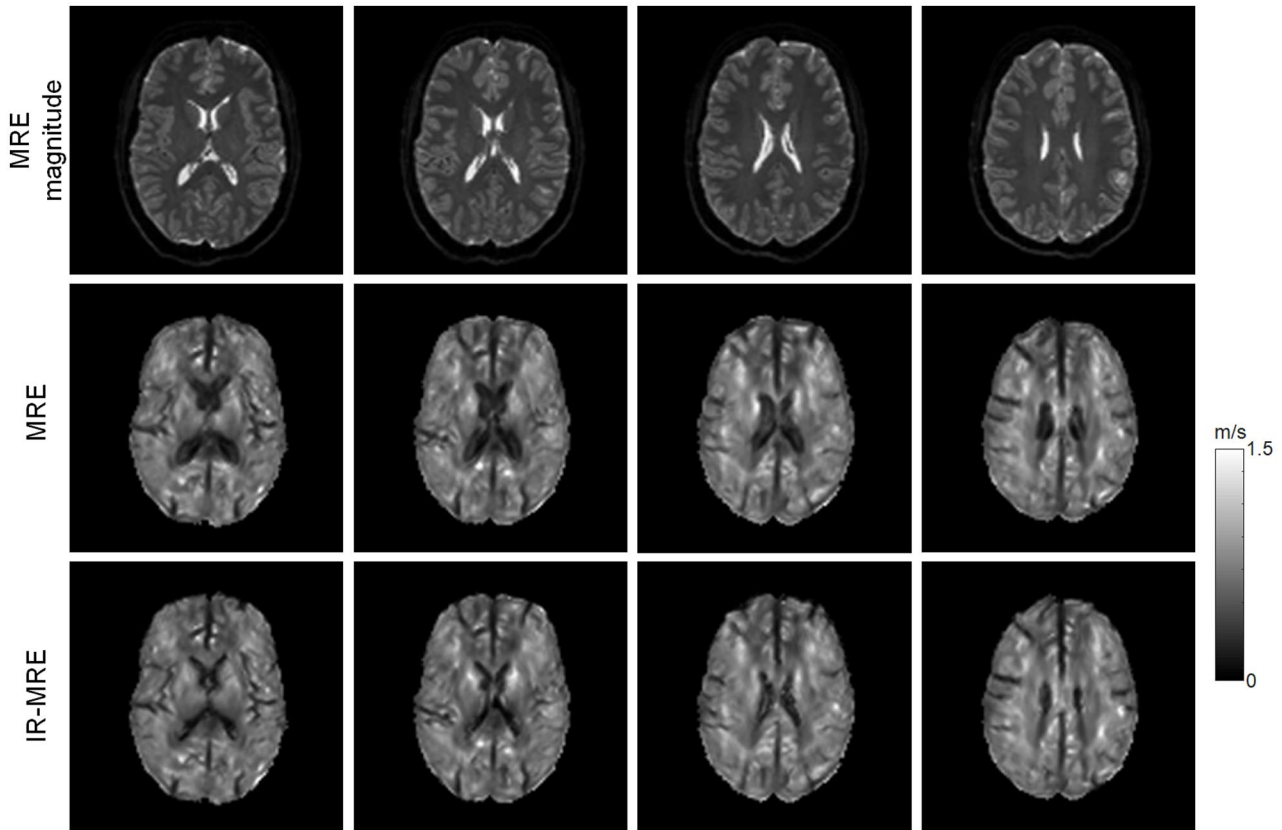
FIGURE 7 Representative SWS maps obtained by MRE and IR-MRE in 1 volunteer. The ventricles appear enlarged in MRE, whereas IR-MRE better depicts ground-truth anatomy as shown by magnitude MRE images
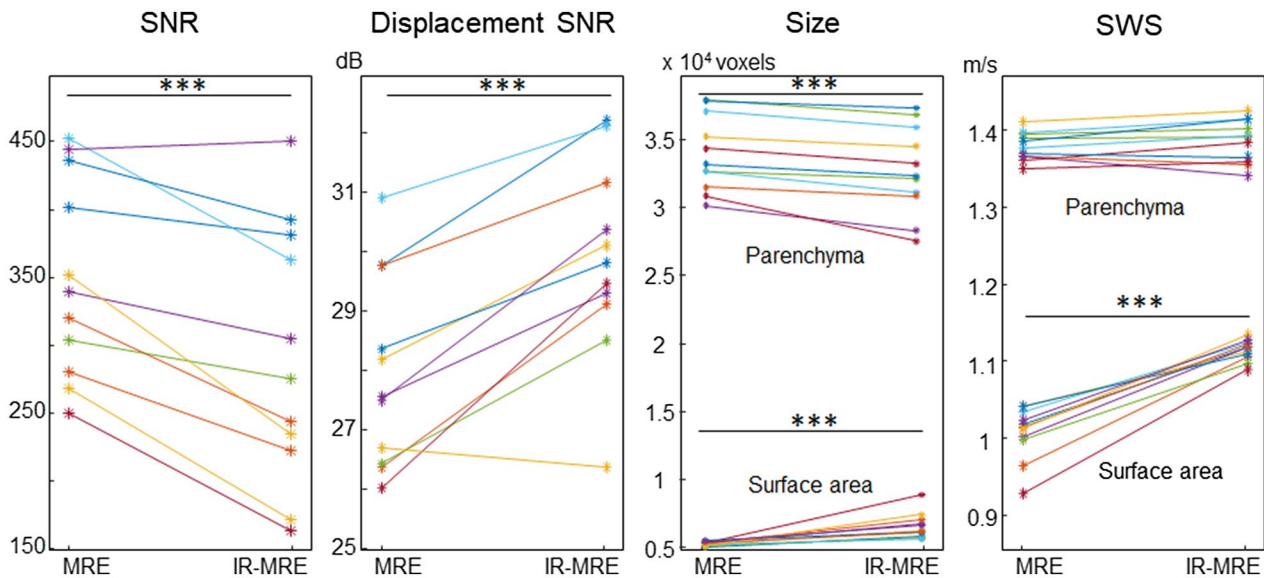

FIGURE 8 Group values of parameters quantified in this study. SNR, SNR derived from the signal magnitudes of brain parenchyma; Displacement SNR, SNR derived from the wave fields within brain tissue; Size, number of voxels covered by the regions of interest of brain tissue and surface areas; SWS, shear wave speed as a marker of stiffness for parenchyma and surface area. ***$P < .001$

of localized properties (partial volume effects) due to inversion.[28] Applied to surface regions in cerebral MRE maps, this partial volume–related averaging of very soft (slip interface) properties of CSF with solid cortex properties results

in overall softening of surface voxels in conventional MRE of the brain. Taken together, fluid–solid interfaces appeared sharper and closer to ground-truth anatomy and have higher stiffness values in IR-MRE than in MRE.

Furthermore, our analysis revealed that bulk parenchyma properties are not different between MRE and IR-MRE. This was expected from our previous work in IR-MRE of the brain, which showed fluid and solid phases in the brain to move in synchrony with identical shear wavelengths and wave phases.[15] Overall, the mean stiffness values we determined fall into the range reported in the literature when converted to shear modulus using the formula $SWS^2 \cdot 1000 \text{ kg/m}^3$, yielding 1.9 ± 0.8 kPa for brain parenchyma and 1.2 ± 0.3 kPa for the cerebral cortex.[1]

While we demonstrated that IR-MRE can suppress CSF signal in the brain, it is conceivable that the technique can also be used to suppress other fluid compartments such as blood in the brain or in other organs such as the liver. However, partial nulling of signal always reduces SNR, which, in our study, was in an acceptable range of approximately 20%, especially as displacement SNR was not affected. Nevertheless, it should be mentioned that, in organs with lower SNR, also displacement SNR might fall below a threshold that may degrade the stability of IR-MRE measurement. Therefore, a careful calibration of displacement SNR and inversion strategy is required when using IR-MRE in other scenarios. A further limitation of IR-MRE is that it requires preparation of magnetization before MRE motion encoding and read-out, which prolongs acquisition time. Our current IR-MRE sequence is a prototype and only applicable for proof-of-concept studies. We used the same sequence in Lilaj et al,[15] in which we systematically validated the suppression of CSF signal in brain tissue and tofu phantoms in a slice-wise fashion using a series of IR times. Use of a single IR time, such as used for CSF-signal suppression in the present experiments, 3D slab IR preparation, and 3D multiband readout would permit a time-efficient preparation and sampling scheme. Because this study focused on a preliminary demonstration of the feasibility of cerebral IR-MRE and stiffness reconstructions in brain surface regions, we will develop accelerated IR-MRE in a future study. Once available, rapid IR-MRE can be applied for multifrequency stimulation and acquisition. Multifrequency IR-MRE is expected to further improve data consistency and enable analysis of tissue viscosity and solid-fluid behavior.[33] We leave this part of MRE parameter reconstruction to future multifrequency IR-MRE studies, because noise-robust k-MDEV inversion provides SWS as a primary parameter, while a second parameter, penetration rate a (also in meters pe second), has been used in only a few studies and was discussed as being prone to geometrical damping.

In summary, IR-MRE is feasible and improves stiffness quantification near fluid–solid boundaries in the human brain. Our results show that IR-MRE preserves ventricle anatomy, provides sharper boundaries in surface areas, and is less affected by fluid vibrations in CSF-filled sulci of the brain, reducing partial volume effects due to inversion-based stiffness reconstruction. The IR-MRE technique provides similar stiffness values as obtained by conventional MRE when applied to bulk tissue, in agreement with the assumption of biphasic, phase-locked shear wave propagation in poroelastic materials. Once improved to be time-efficient, IR-MRE could be extended to multifrequency data acquisition and become a valuable method for consistent viscoelastic property quantification in the human brain.

ORCID
Ledia Lilaj https://orcid.org/0000-0001-8222-0397
Helge Herthum https://orcid.org/0000-0001-6494-0833
Mehrgan Shahryari https://orcid.org/0000-0002-3981-1711
Jürgen Braun https://orcid.org/0000-0001-5183-7546
Sebastian Hirsch https://orcid.org/0000-0001-8187-8242
Ingolf Sack https://orcid.org/0000-0003-2460-1444

REFERENCES

1. Hiscox LV, Johnson CL, Barnhill E, et al. Magnetic resonance elastography (MRE) of the human brain: technique, findings and clinical applications. *Phys Med Biol*. 2016;61:R401-R437.
2. Yin Z, Romano AJ, Manduca A, Ehman RL, Huston J 3rd. Stiffness and beyond: what MR elastography can tell us about brain structure and function under physiologic and pathologic conditions. *Top Magn Reson Imaging*. 2018;27:305-318.
3. Johnson CL, Telzer EH. Magnetic resonance elastography for examining developmental changes in the mechanical properties of the brain. *Dev Cogn Neurosci*. 2018;33:176-181.
4. Hirsch S, Braun J, Sack I. *Magnetic Resonance Elastography: Physical Background and Medical Applications*. Weinheim, Germany: Wiley-VCH; 2017.
5. Doyley MM. Model-based elastography: a survey of approaches to the inverse elasticity problem. *Phys Med Biol*. 2012;57:R35-R73.
6. Manduca A, Bayly PJ, Ehman RL, et al. MR elastography: principles, guidelines, and terminology. *Magn Reson Med*. 2021;85:2377-2390.
7. Fovargue D, Nordsletten D, Sinkus R. Stiffness reconstruction methods for MR elastography. *NMR Biomed*. 2018;31:e3935.
8. Budday S, Ovaert TC, Holzapfel GA, Steinmann P, Kuhl E. Fifty shades of brain: a review on the mechanical testing and modeling of brain tissue. *Arch Comput Methods Eng*. 2020;27:1187-1230.
9. Braun J, Guo J, Lützkendorf R, et al. High-resolution mechanical imaging of the human brain by three-dimensional multifrequency magnetic resonance elastography at 7T. *Neuroimage*. 2014;90:308-314.
10. McGarry M, Van Houten E, Solamen L, Gordon-Wylie S, Weaver J, Paulsen K. Uniqueness of poroelastic and viscoelastic nonlinear inversion MR elastography at low frequencies. *Phys Med Biol*. 2019;64:075006.
11. Perrinez PR, Kennedy FE, Van Houten EE, Weaver JB, Paulsen KD. Modeling of soft poroelastic tissue in time-harmonic MR elastography. *IEEE Trans Biomed Eng*. 2009;56:598-608.
12. Perrinez PR, Kennedy FE, Van Houten EE, Weaver JB, Paulsen KD. Magnetic resonance poroelastography: an algorithm for

estimating the mechanical properties of fluid-saturated soft tissues. *IEEE Trans Med Imaging*. 2010;29:746-755.

13. Hirsch S, Klatt D, Freimann F, Scheel M, Braun J, Sack I. In vivo measurement of volumetric strain in the human brain induced by arterial pulsation and harmonic waves. *Magn Reson Med*. 2012;70:671-683.

14. Hirsch S. A biphasic poroelastic model for soft tissues. In: Sack I, Schaeffter T, eds. *Quantification of Biophysical Parameters in Medical Imaging*, 1st Edition. Heidelberg, Germany: Springer; 2018:71.

15. Lilaj L, Fischer T, Guo J, Braun J, Sack I, Hirsch S. Separation of fluid and solid shear wave fields and quantification of coupling density by magnetic resonance poroelastography. *Magn Reson Med*. 2021;85:1655-1668.

16. Papazoglou S, Hamhaber U, Braun J, Sack I. Horizontal shear wave scattering from a nonwelded interface observed by magnetic resonance elastography. *Phys Med Biol*. 2007;52:675-684.

17. Biot MA. Theory of propagation of elastic waves in a fluid-saturated porous solid. 1. Low-frequency range. *J Acoust Soc Am*. 1956;28:168-178.

18. Elgeti T, Rump J, Papazoglou S, et al. Cardiac magnetic resonance elastography—initial results. *Invest Radiol*. 2008;43: 762-772.

19. Kolipaka A, McGee KP, Manduca A, Anavekar N, Ehman RL, Araoz PA. In vivo assessment of MR elastography-derived effective end-diastolic myocardial stiffness under different loading conditions. *J Magn Reson Imaging*. 2011;33:1224-1228.

20. Arani A, Arunachalam SP, Chang ICY, et al. Cardiac MR elastography for quantitative assessment of elevated myocardial stiffness in cardiac amyloidosis. *J Magn Reson Imaging*. 2017;46:1361-1367.

21. Kolipaka A, Woodrum D, Araoz PA, Ehman RL. MR elastography of the in vivo abdominal aorta: a feasibility study for comparing aortic stiffness between hypertensives and normotensives. *J Magn Reson Imaging*. 2012;35:582-586.

22. Schaafs LA, Schrank F, Warmuth C, et al. Steady-state multifrequency magnetic resonance elastography of the thoracic and abdominal human aorta-validation and reference values. *Invest Radiol*. 2020;55:451-456.

23. Tzschatzsch H, Guo J, Dittmann F, et al. Tomoelastography by multifrequency wave number recovery from time-harmonic propagating shear waves. *Med Image Anal*. 2016;30:1-10.

24. Ariyurek C, Tasdelen B, Ider YZ, Atalar E. SNR weighting for shear wave speed reconstruction in tomoelastography. *NMR Biomed*. 2021;34:e4413.

25. Schrank F, Warmuth C, Tzschatzsch H, et al. Cardiac-gated steady-state multifrequency magnetic resonance elastography of the brain: effect of cerebral arterial pulsation on brain viscoelasticity. *J Cereb Blood Flow Metab*. 2020;40:991-1001.

26. Herthum H, Shahryari M, Tzschätzsch H, et al. Real-time multifrequency MR elastography of the human brain reveals rapid changes in viscoelasticity in response to the Valsalva Maneuver. *Front Bioeng Biotechnol*. 2021;9:666456.

27. Shahryari M, Meyer T, Warmuth C, et al. Reduction of breathing artifacts in multifrequency magnetic resonance elastography of the abdomen. *Magn Reson Med*. 2021;85:1962-1973.

28. Mura J, Schrank F, Sack I. An analytical solution to the dispersion-by-inversion problem in magnetic resonance elastography. *Magn Reson Med*. 2020;84:61-71.

29. Donoho DL, Johnstone IM, Kerkyacharian G, Picard D. Wavelet shrinkage—asymptopia. *J R Stat Soc Series B Methodol*. 1995;57:301-337.

30. Bertalan G, Guo J, Tzschatzsch H, et al. Fast tomoelastography of the mouse brain by multifrequency single-shot MR elastography. *Magn Reson Med*. 2019;81:2676-2687.

31. Papazoglou S, Xu C, Hamhaber U, et al. Scatter-based magnetic resonance elastography. *Phys Med Biol*. 2009;54:2229-2241.

32. Yin Z, Glaser KJ, Manduca A, et al. Slip interface imaging predicts tumor-brain adhesion in Vestibular Schwannomas. *Radiology*. 2015;277:507-517.

33. Streitberger KJ, Lilaj L, Schrank F, et al. How tissue fluidity influences brain tumor progression. *Proc Natl Acad Sci USA*. 2020;117:128-134.

SUPPORTING INFORMATION

Additional Supporting Information may be found online in the Supporting Information section.

FIGURE S1 Shear wave speed (SWS) maps of the two phantoms shown in Figure 3A,B are preprocessed by masking out the fluid and air areas before inversion. Artifacts that appear around the phantoms are related to discontinuities introduced by the masks. This demonstrates that simple masking of fluid regions does not offer additional insights, whereas inversion-recovery MR elastography (IR-MRE) improves the characterization of boundaries by intrinsically suppressing the signal of fluid oscillations

> **How to cite this article:** Lilaj L, Herthum H, Meyer T, et al. Inversion-recovery MR elastography of the human brain for improved stiffness quantification near fluid–solid boundaries. *Magn Reson Med*. 2021;86:2552–2561. https://doi.org/10.1002/mrm.28898